

Improved body quantitative susceptibility mapping by using a variable-layer single-min-cut graph-cut for field-mapping

Christof Boehm¹   | Maximilian N. Diefenbach^{1,2}  | Marcus R. Makowski¹ | Dimitrios C. Karampinos¹

¹Department of Diagnostic and Interventional Radiology, Technical University of Munich, Munich, Germany

²Division of Infectious Diseases and Tropical Medicine, University Hospital, LMU Munich, Munich, Germany

Correspondence

Christof Boehm, Department of Diagnostic and Interventional Radiology, Klinikum rechts der Isar, Ismaninger Str 22, 81675 Munich, Germany.

Email: christof.boehm@tum.de

Purpose: To develop a robust algorithm for field-mapping in the presence of water–fat components, large B_0 field inhomogeneities and MR signal voids and to apply the developed method in body applications of quantitative susceptibility mapping (QSM).

Methods: A framework solving the cost-function of the water–fat separation problem in a single-min-cut graph-cut based on the variable-layer graph construction concept was developed. The developed framework was applied to a numerical phantom enclosing an MR signal void, an air bubble experimental phantom, 14 large field of view (FOV) head/neck region *in vivo* scans and to 6 lumbar spine *in vivo* scans. Field-mapping and subsequent QSM results using the proposed algorithm were compared to results using an iterative graph-cut algorithm and a formerly proposed single-min-cut graph-cut.

Results: The proposed method was shown to yield accurate field-map and susceptibility values in all simulation and *in vivo* datasets when compared to reference values (simulation) or literature values (*in vivo*). The proposed method showed improved field-map and susceptibility results compared to iterative graph-cut field-mapping especially in regions with low SNR, strong field-map variations and high R_2^* values.

Conclusions: A single-min-cut graph-cut field-mapping method with a variable-layer construction was developed for field-mapping in body water–fat regions, improving quantitative susceptibility mapping particularly in areas close to MR signal voids.

KEY WORDS

chemical shift encoding-based water–fat separation, Dixon imaging, field-mapping, graph-cuts, quantitative susceptibility mapping

[Correction statement: Correction added after online publication November 30, 2020. Due to a publisher error, the article was published online before all corrections were implemented. This version shows the correct figures with the correct captions, corrections to equations 1 and 6, and several minor text edits.]

This is an open access article under the terms of the Creative Commons Attribution-NonCommercial License, which permits use, distribution and reproduction in any medium, provided the original work is properly cited and is not used for commercial purposes.

© 2020 The Authors. *Magnetic Resonance in Medicine* published by Wiley Periodicals LLC on behalf of International Society for Magnetic Resonance in Medicine

1 | INTRODUCTION

Quantitative susceptibility mapping (QSM)¹ is an MR technique directly probing a fundamental tissue property, the magnetic susceptibility. QSM is an emerging imaging method in the study of brain physiology,² pathology,³ and function.⁴ QSM has been also recently applied in tissues outside the brain, for example, for measuring liver iron overload,⁵⁻⁷ prostatic calcifications,⁸ cartilage degeneration,⁹ and bone density.^{10,11} The main premise of QSM is that it overcomes limitations of R_2^* -mapping by distinguishing between para- and diamagnetic susceptibility sources, which would similarly result in increased R_2^* values.¹² Furthermore, recent studies have shown that QSM may lead to a reduced dependence on the microscopic distribution of the bone marrow bone microstructure¹³ or the microscopic distribution of iron¹⁴ compared to R_2^* -map.

QSM inverts the measured main magnetic field inhomogeneities, the so-called *field-map*, to the magnetic susceptibility map. When applied in body regions, QSM processing needs to particularly address the presence of fat with its chemical shift effect.⁵ The first QSM step, the magnetic field-mapping, therefore connects QSM to the sub-domain of chemical shift encoding-based water–fat separation, which also can be reformulated as a field-map estimation problem.^{5,11,15} Field-mapping in the body can be challenging for mainly two reasons: (a) the presence of large background fields possibly due to concave geometry of the anatomy or air inclusions in the field of view (FOV),¹⁶ and (b) the presence of signal voids in regions of low signal-to-noise ratio (SNR) due to MR invisible or short- T_2 tissues, for example, bone.¹⁷ Field-mapping in water–fat regions relies on optimizing a least-squares optimization problem due to the nonlinearity of the field-map term.^{5,18,19} Most methods previously proposed for solving the above non-convex optimization problem have been investigated in terms of the achieved accuracy on the water- and fat-separated images and not on the field-map. In water–fat imaging, the field-map is typically treated as a nuisance parameter, whereas in QSM the field-map is of central importance.

Most existing approaches proposed to solve the water–fat separation problem have been relying on a smoothness constraint on the field-map^{18,20-22} and some of them were incorporated in the 2012 ISMRM fat–water toolbox.²³ Algorithms formulating the water–fat separation problem as a graph search have been particularly successful in solving the constrained optimization problem using either min-cuts iteratively²⁰ or single-min-cut approaches.^{24,25} The formulation of the water–fat separation problem as a graph search was first introduced in the seminal work by Hernando et al.,²⁰ showing excellent water–fat separation results and was included in the 2012 ISMRM fat–water toolbox. Specifically, for each voxel, only two field-map candidates are taken and

a graph-cut is used to solve the cost function in a so-called jump move. If the cost function decreases, the field-map candidate is taken. This procedure is repeated until a defined convergence criterion is met and the method is therefore labeled as an iterative graph-cut approach (iGC). However, the original iterative graph-cut in²⁰ does not necessarily converge to the global minimum of its defined cost function, smoothes the field-map by construction and allows for adopting only two-dimensional neighborhood information in the field-map smoothness constraint term (interslice regularization is not possible). A single-min-cut graph-cut can address the above problems of the iterative graph-cut technique and guarantees to find the globally optimal solution. A single-min-cut graph-cut method, labeled as *rapid globally optimal surface estimation* (rGOOSE)²⁵ was recently introduced and proposed to restrict the field-map candidates to be only local minima of the voxel-wise field-map estimate. However, rGOOSE allows for the same amount of minima per voxel for the whole volume and includes the residual error of each minima in the global cost function similarly to the iterative graph-cut. Therefore, rGOOSE is associated with long computation times and can in some cases miss the optimal solution due to its graph construction.

Therefore, the purpose of the present work is (a) to develop an accelerated single-min-cut graph-cut algorithm for field-mapping in the presence of water–fat using a variable-layer graph construction and (b) to demonstrate the advantages of the developed field-mapping technique when applied for body QSM in the presence of large background fields and signal voids. The ability of the proposed variable-layer graph-cut (vlGC) based algorithm to overcome limitations of current state-of-the-art body field-mapping methods is particularly examined with simulations and in vivo measurements of body QSM.

2 | THEORY

2.1 | Cost function of the water–fat separation problem

Assuming the widely used single- R_2^* multi-fat-peak water–fat voxel signal model,^{26,27} the complex signal at the n -th echo is

$$\begin{aligned} s_{\text{model}}(t_n) &= (\rho_W + c_n \rho_F) e^{i \gamma t_n}, \quad \gamma = i 2 \pi f_B - R_2^* \\ c_n &= \sum_{p=1}^P a_p e^{i 2 \pi \Delta f_p t_n}, \quad \text{with } \sum_{p=1}^P a_p = 1, \end{aligned} \quad (1)$$

with t_1, t_2, \dots, t_N the different echo times, f_B the local frequency shift due to static field inhomogeneity and ρ_W and ρ_F the complex signal of the water and fat components assuming to have an equal transverse relaxation rate R_2^* . The fat spectrum

is assumed to have P spectral peaks with corresponding relative amplitudes a_p and chemical shift Δf_p . The above signal model can be rewritten into its matrix representation^{24,28}:

$$\underbrace{\begin{pmatrix} e^{\gamma t_1} & e^{\gamma t_1} \sum_{p=1}^P a_p e^{i2\pi(\Delta f_p)t_1} \\ \vdots & \vdots \\ e^{\gamma t_n} & e^{\gamma t_n} \sum_{p=1}^P a_p e^{i2\pi(\Delta f_p)t_n} \end{pmatrix}}_{\Psi_\gamma} \underbrace{\begin{pmatrix} \rho_W \\ \rho_F \\ \rho \end{pmatrix}}_{\boldsymbol{\rho}} = \underbrace{\begin{pmatrix} y(t_1) \\ \vdots \\ y(t_n) \end{pmatrix}}_{\mathbf{y}}. \quad (2)$$

When the fat spectrum and its relative amplitudes are assumed to be known, the remaining unknown parameters are obtained by minimizing the least-squares error between the model and the measured data:

$$\{\rho_W, \rho_F, \gamma\} = \arg \min_{\rho_W, \rho_F, \gamma} \|\Psi_\gamma \boldsymbol{\rho} - \mathbf{y}\|_2^2. \quad (3)$$

Since the above voxel-wise minimization problem depends on many parameters the VARPOR¹⁹ approach is used to decouple them. Specifically, the above least-squares error is minimized with respect to some of the variables by assuming the others to be fixed. Minimizing the above cost function with respect to the complex water and fat signal $\boldsymbol{\rho}^0$ assuming γ to be fixed, the signal estimates as $\boldsymbol{\rho}^0 = (\Psi_\gamma^T \Psi_\gamma)^{-1} \Psi_\gamma^T \mathbf{y}$. Substituting $\boldsymbol{\rho}^0$ back in Equation (3), and solving for γ , we obtain²⁴:

$$\gamma(\mathbf{r}) = \operatorname{argmin}_{\gamma} \underbrace{\|\Psi_\gamma (\Psi_\gamma^T \Psi_\gamma)^{-1} \Psi_\gamma^T \mathbf{y}(\mathbf{r}) - \mathbf{y}(\mathbf{r})\|_2^2}_{\mathcal{D}(\mathbf{r}, \gamma)}. \quad (4)$$

To obtain a cost function that is only dependent on f_B the above expression can again be minimized with respect to R_2^* ²⁴:

$$f_B^0 = \operatorname{argmin}_{f_B} \underbrace{\min_{R_2^*} \mathcal{D}(\mathbf{r}, \gamma)}_{C(f_B(\mathbf{r}))}. \quad (5)$$

However, minimizing $C(f_B)$ voxel by voxel is undesirable, because C has several local and global minima,^{18,29} is non-convex, periodic in the field-map dimension and sensitive to noise. Therefore, a penalized maximum likelihood cost function is employed and minimized allowing to impose spatial smoothness:

$$\hat{f}_B = \operatorname{argmin}_{f_B(\mathbf{r})} \sum_{\mathbf{r}} \sum_{\mathbf{s} \in N(\mathbf{r})} |f_B(\mathbf{r}) - f_B(\mathbf{s})|^2, \quad (6)$$

where $f_B(\mathbf{r})$ is the field-map. At each voxel \mathbf{r} , field-map values are restricted to only local minimizers of $C(f_B(\mathbf{r}))$. The restriction to only local minimizers solely enforces the data consistency. $N(\mathbf{r})$ is the voxel neighborhood that has to be selected. Furthermore, the minimization of Equation (6) is restricted to signal only regions by setting:

$$\mathbf{r} \in M \text{ and } M = \{(x, y, z) \mid \text{MIP}_{\text{TE}}(x, y, z) > T\}, \quad (7)$$

where T is a threshold which needs to be chosen appropriately and MIP_{TE} is the the maximum intensity projection of the signal over echo times.

2.1.1 | The sampling interval of the voxel independent field-mapping estimate

The voxel maximum likelihood estimate Equation (5) is periodic in the field-map dimension for equidistant echo times t_n with a period length of:

$$f_{\text{period}} = \frac{1}{\Delta \text{TE}} = \frac{1}{t_{n+1} - t_n}, \quad (8)$$

where ΔTE is the echo time step. This is the bandwidth of the field-map that should at least be sampled to obtain every existing local and global minima per voxel. The number of minima at each voxel depends on the fat model, the number of recorded echoes and the measured signal.

When two adjacent voxels v_1, v_2 whose signal only differs in their field-map value f_{B_1}, f_{B_2} are considered, the sampling bandwidth of Equation (8) needs to be extended to:

$$f_{\text{total}} = f_{\text{period}} + |f_{B_1} - f_{B_2}|, \quad (9)$$

to ensure that every minima at each voxel is correctly encoded into the graph without a false value in the penalization term. If the sampling interval was chosen too small, a minima would be wrapped around to the other end of the interval due to the periodicity in the field-map dimension.

The above idea can be generalized to an arbitrary number of voxels:

$$f_{\text{total}} = f_{\text{period}} + |\max(\hat{f}_B) - \min(\hat{f}_B)|, \quad (10)$$

where $\max(\hat{f}_B)$ and $\min(\hat{f}_B)$ are the maximum and minimum value of the global field-map estimate, respectively.

The sampling interval is finally defined as the above total bandwidth centered around zero:

$$f_{\text{sampling}} = \left[-\frac{f_{\text{total}}}{2}, \frac{f_{\text{total}}}{2} \right]. \quad (11)$$

3 | METHODS

A novel field-mapping algorithm was first developed based on a variable-layer graph construction concept and the novel formulation of the data consistency as introduced in Equation (6). The developed method was then applied to a numerical

phantom, an experimental phantom, in vivo large FOV head/neck scans and in vivo spine scans and compared to the state-of-the-art iGC method from²⁰ as included in the ISMRM fat-water toolbox²³ and the previously proposed single-min-cut graph-cut rGOOSE method.²⁵

3.1 | Proposed single-min-cut variable-layer graph-cut algorithm

The maximum intensity projection across echoes MIP_{TE}, thresholded at 5% of its maximum value, was used to distinguish between signal and no-signal regions for the mask (see Equation 7). In the calculation of the VARPRO residual, a sampling step size of 2 Hz was used, defined empirically in order to keep the discretization error reasonably small.¹⁹ The residual was computed over the period defined in Equation (8) and replicated until it matched the sampling interval defined in Equation (11). To determine the sampling interval, max(\hat{f}_B) and min(\hat{f}_B) in Equation (10) needed to be estimated. This was done by choosing the central slice of the volume and using a large sampling interval such that the range of field-map values in the slice lies within this interval. The proposed vIGC was subsequently applied on the central slice with the large sampling interval and max(\hat{f}_B) and min(\hat{f}_B) were extracted. The voxel-wise residuals were then computed for the whole volume for the sampling interval determined by max(\hat{f}_B) and min(\hat{f}_B). All local and global minima per voxel were finally extracted using MATLAB (R2017b, MathWorks) built-in functions.

The minimization of the global maximum likelihood cost function defined in Equation (6) can be transformed into a surface estimation problem using the graph-cut algorithm introduced in.³⁰ The graph-cut algorithm in³⁰ was designed for graphs with irregularly sampled spacings and a convex regularization term (quadratic distance measure in the present setting) and hence guarantees the convergence to the global

minimum of Equation (6). The ability of the algorithm to incorporate irregularly sampled spacings is necessary since the frequency distance of the extracted local and global minima in the present problem is typically not equidistant. Based on the cost function values for the set of local minima at each voxel, the graph was constructed. Since each node needs to be identifiable, each node was assigned with a distinct identification number (ID). The order x, y, z , frequency was used to create a node index array. Lists with all edges were next calculated and transformed into a equivalent sparse adjacency matrix, which fully defined the graph. Figure 1 shows an example of the constructed graph for two adjacent voxels. Edges between nodes were calculated according to.³⁰ The MATLAB-implementation of the Boykov-Kolmogorov max-flow algorithm was applied on the constructed graph. The above algorithm was found to be most efficient to solve graph-cut problems like the mapping of a cost function similar to the proposed global cost function.³¹ Boykov-Kolmogorov max-flow algorithm returned the max-flow in the network (which was of no further interest) and two lists of node IDs belonging either to the source or to the terminal node. The graph was constructed based on the convention introduced in³⁰ that the highest ID in a voxel belonging to the subset of the source was the searched solution.

3.2 | Speed comparison

The vIGC was compared to the former proposed single-min-cut graph-cut algorithm rGOOSE.²⁵ Therefore, the three central slices of a head/neck region were selected (please see below for details). The vIGC was applied to obtain a reference field-map and run-time. The rGOOSE method was repeatedly applied to the dataset while increasing the number of layers at each iteration from 1 to 30. The resulting run-time was normalized with the run-time from the vIGC to increase system comparability. Since the absolute error is

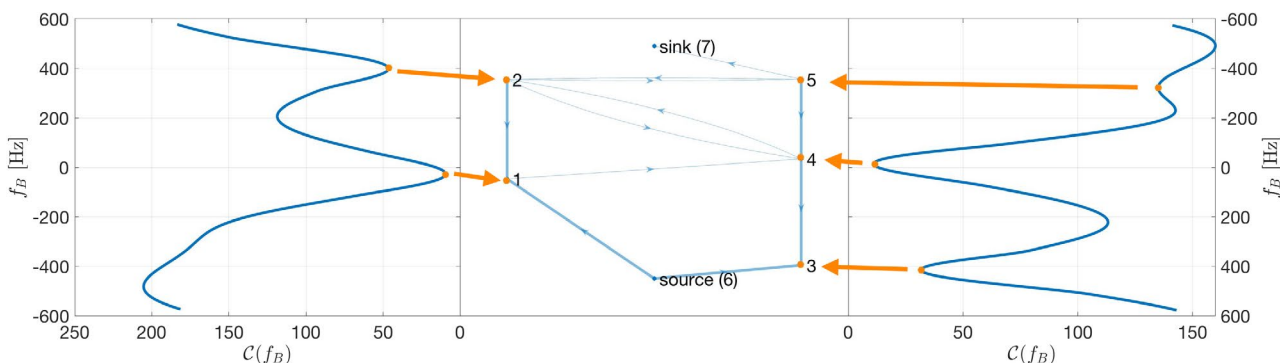


FIGURE 1 Variable-layer graph construction in 2 adjacent voxels arbitrarily extracted from one lumbar spine dataset. The voxel-wise field-mapping estimate $C(f_B)$ is sampled over the same interval in both voxels, resulting in 2 and 3 minima, respectively, as illustrated in the left and right plots. From $C(f_B)$ only the local minima are extracted and encoded in the graph as illustrated in the center plot. The edges in the graph are calculated according to³⁰

of no interest, the error between the reference and the field-map yielded by rGOOSE was determined by computing the normalized root mean square error (NRMSE) between both and rescaling it into % of its maximum value. The methods were run on a 2017's iMac with a 4.2 GHz CPU (Intel Core i7, 7700, 4 processors) and 32 GiB RAM. Additionally, the run-time of the iGC, the rGOOSE method, and the vIGC were measured for the field-map estimation of the numerical phantom with the sharp air-tissue interface (please see details below).

3.3 | Air bubble phantom: Numerical simulation and experimental measurement

To investigate the behavior of the developed field-mapping method close to signal voids (eg air inclusions), a numerical phantom with an air bubble in the center, surrounded by a tissue with fat fraction of 30% was set up. A $\text{FOV} = 128 \times 128 \times 60 \text{ mm}^3$, an isotropic voxel size = $1 \times 1 \times 1 \text{ mm}^3$ and a single $R_2^* = 40 \text{ Hz}$ for the whole volume were used. The radius of the air bubble was set to $r = 20 \text{ mm}$. The phantom generation was performed twice: once with a sharp air-tissue interface and once with a smooth air-tissue interface. By applying a Gaussian filter with a standard deviation of $\sigma = 6$ and a mean of $\mu = 0$ the interface from air to tissue was smoothed out to have a continuous transition. A χ -map with $\chi_{\text{air}} = 9 \text{ ppm}$ and $\chi_{\text{fat}} = 0.6 \text{ ppm}$ in reference to $\chi_{\text{water}} = 0$ was created. In the area of the transition, Wiedemanns additive law was used to calculate the χ values accordingly.³² Wiedemanns additive law states that the overall magnetic susceptibility of a mixture is the weighted sum of the magnetic susceptibilities of the constituents. A corresponding field-map was then forward simulated. With the echo times $\text{TE} = [2.2, 3.4, 4.6, 5.8, 7.0, 8.2] \text{ ms}$, a field strength of 3 T and a multi-peak fat model specific to bone marrow³³ the signal was also forward simulated using the signal model displayed in Equation (1).

The numerical phantom signal values were used to evaluate the performance of the iGC algorithm and of the developed single-min-cut graph-cut algorithm first for field-mapping. The computed field-maps were subsequently used for QSM processing. The QSM processing used for the dipole inversion a closed-form ℓ_2 -regularized algorithm without data weighting as in.³⁴ Field-mapping and QSM processing were performed for both the phantom with the smooth air-tissue interface and the phantom with the sharp air-tissue interface. The field-mapping results comparison was based on the results from the phantom with the smooth air-tissue interface to especially examine partial volume effects close to signal voids. The QSM comparison was based on the results from the phantom with the sharp air-tissue interface to assure edge preservation.

To validate the numerical simulation, an air bubble phantom was built consisting of an air-containing ball with a thin plastic shell and a radius of $r = 20 \text{ mm}$ placed in the center of a large water reservoir. Scanning was performed on a 3 T scanner (Ingenia, Philips Healthcare, Release 5.4, Best, The Netherlands) using a monopolar time-interleaved multi-echo gradient echo sequence,³⁵ acquiring 6 echoes with 3 echoes per interleave. $\text{TE}_{\min} = 1.12 \text{ ms}$, $\Delta \text{TE} = 0.98 \text{ ms}$, orientation = coronal, readout direction = feet-head, and an isotropic acquisition voxel size of 1.5 mm in every dimension. The phantom was repeatedly scanned varying the shimming parameters from no shimming to only a linear shimming field in z-direction of $B_{0,\text{shimming}(z)} = [0.2, 0.4, 0.6] \text{ mT/m}$. To obtain susceptibility maps the pipeline of the numerical simulation was used in addition to the Laplacian boundary value method³⁶ to remove the background fields.

3.4 | In vivo measurements

The vIGC was applied to in vivo scans of both healthy volunteers and patients. Approval by the institutional review board (Klinikum Rechts der Isar, Technical University of Munich, Munich, Germany) was granted beforehand and informed written consent was obtained from all scanned volunteers and patients. Scanning was performed on the aforementioned 3 T scanner.

Specifically, 14 scans of the head/neck region of healthy volunteers, scans of the lumbar spine of 4 healthy volunteers and scans of the lumbar spine of two osteoporotic patients were evaluated.

The head/neck region was selected as a region with large B_0 inhomogeneities to assess the performance of the vIGC in field-mapping of regions with a rapidly spatially varying field-map. A monopolar multi-echo gradient echo sequence with 3 echoes acquired in a single TR was used³⁵ with $\text{TE}_{\min} = 1.06 \text{ ms}$, $\Delta \text{TE} = 1.59 \text{ ms}$, orientation = coronal, readout direction = feet-head, $\text{FOV} = 480 \times 480 \times 224 \text{ mm}^3$ and acquisition voxel size = $2 \times 2 \times 4 \text{ mm}^3$.

The lumbar spine was selected to assess the performance of the vIGC on field-mapping used for subsequent QSM processing. For the spine scans, the aforementioned monopolar time-interleaved multi-echo gradient echo sequence was used. For the osteoporotic spine, imaging parameters were set to $\text{TE}_{\min} = 1.33 \text{ ms}$, $\Delta \text{TE} = 1.08 \text{ ms}$, orientation = sagittal, readout direction = anterior-posterior, $\text{FOV} = 220 \times 220 \times 79.2 \text{ mm}^3$, acquisition voxel size of 1.8 mm³ isotropic and for the healthy spines to $\text{TE}_{\min} = 1.12 \text{ ms}$, $\Delta \text{TE} = 0.87 \text{ ms}$, orientation = sagittal, readout direction = anterior-posterior, $\text{FOV} = 220 \times 220 \times 79.2 \text{ mm}^3$ and acquisition voxel size of 1.8 mm³ isotropic. For QSM processing

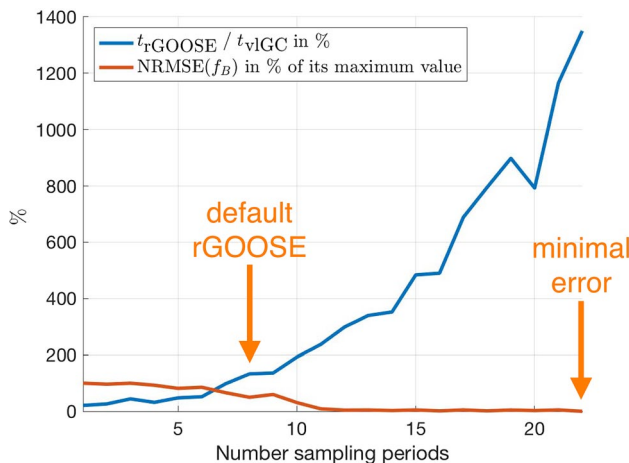


FIGURE 2 Speed comparison of the vlGC to a previously proposed single-min-cut graph-cut method (rGOOSE).²⁵ The underlying dataset is one of the head/neck datasets. With increasing layers in rGOOSE the resulting field-map converges to the field-map of the vlGC. When the difference between the two methods becomes minimal, rGOOSE takes 14 times as long as the vlGC. In²⁵ it was suggested to use 8 layers in the graph, this point is indicated in the plot and represents a suboptimal solution

in the lumbar vertebral column region, an algorithm with joint background field removal and dipole inversion was used solving the following ℓ_1 total-variation regularized optimization problem³⁷:

$$\chi = \arg \min_{\chi'} \left\| W \Delta \left(f_B - \frac{\gamma}{2\pi} B_0 d * \chi' \right) \right\|_2 + \lambda \| M \nabla \chi' \|_1, \quad (12)$$

where f_B is the field-map estimate, the Larmor frequency $\frac{\gamma}{2\pi} B_0$, dipole kernel d , magnitude weighting W , and a MEDI-like edge regularization damping M .¹ The joint background field and dipole inversion method has been chosen since it does not require the definition of a background and foreground region-of-interest in order to perform the background field removal. To evaluate the quantitative performance of the performed QSM, the susceptibility values of the spinous process cortical bone region were determined in all subjects. Specifically, the ROIs were manually drawn in the cortical bone sites of the spinous process at the level of the L3 lumbar vertebral body. In addition, one subject was re-positioned and re-scanned to assess the repeatability of the estimated spinous process magnetic susceptibility.

3.5 | In vivo field-mapping consistency check

An obvious challenge while comparing the performance of different field-mapping methods *in vivo* is the absence of an established gold-standard measurement of the field-map. A heuristic method to verify correct field-mapping is the

examination of the water–fat separated images, as applied in previous works. Given anatomical prior knowledge, it should be known which anatomy is mainly water- or fat-containing. Based on the above knowledge, the corresponding water–fat images were checked if the separation has correctly worked. All head/neck datasets processed with both the iGC and the vlGC were visually rated and categorized in results with and without water–fat swaps, where regions in the heart and only a few voxels close to the object boundaries were not regarded. The overall counts of datasets with and without residual water–fat swaps served as a more global metric on how the vlGC performed in a challenging anatomy across all 14 datasets.

4 | RESULTS

4.1 | Speed comparison

Figure 2 compares the computational speed of the rGOOSE method to the speed of the vlGC. The three central slices of one head/neck region were selected for the speed comparison. With increasing number of layers the run-time of rGOOSE drastically increases and the difference between the field-map obtained by the rGOOSE compared to the field-map obtained by the vlGC decreases. The difference between the two methods becomes minimal from 22 layers, where the computational time for the rGOOSE is 14 times longer than the computational time for the vlGC. In absolute time units, the rGOOSE requires 1 hr 31 mins and the vlGC requires 7 mins.

4.2 | Air bubble phantom: Numerical simulation and experimental measurement

Figure 3 compares the field-mapping accuracy of the different methods in the numerical phantom. The field-map obtained by the iGC shows significant errors particular close to the signal void in the center of the volume (region with a small MR signal due to the simulated partial voluming effect) and a strong ring-shaped artifact reaching to the borders of the volume. The field-map from the iGC shows primarily larger errors in regions with small MR signal. The field-map obtained by the vlGC shows errors smaller than the field-map discretization step throughout the volume. The field-mapping errors propagate into the water–fat separated images. The error maps of the water–fat separated images from the iGC show a ring-shaped artifact, similar to the field-map, and largest errors close to the signal void. The above errors of the iGC lead to a significant false estimation of the water and fat components and to partial swaps, whereas the vlGC shows negligible errors and no swaps.

The first row of Figure 4 shows the field-maps of the iGC, rGOOSE and the vlGC in the sharp boundary numerical

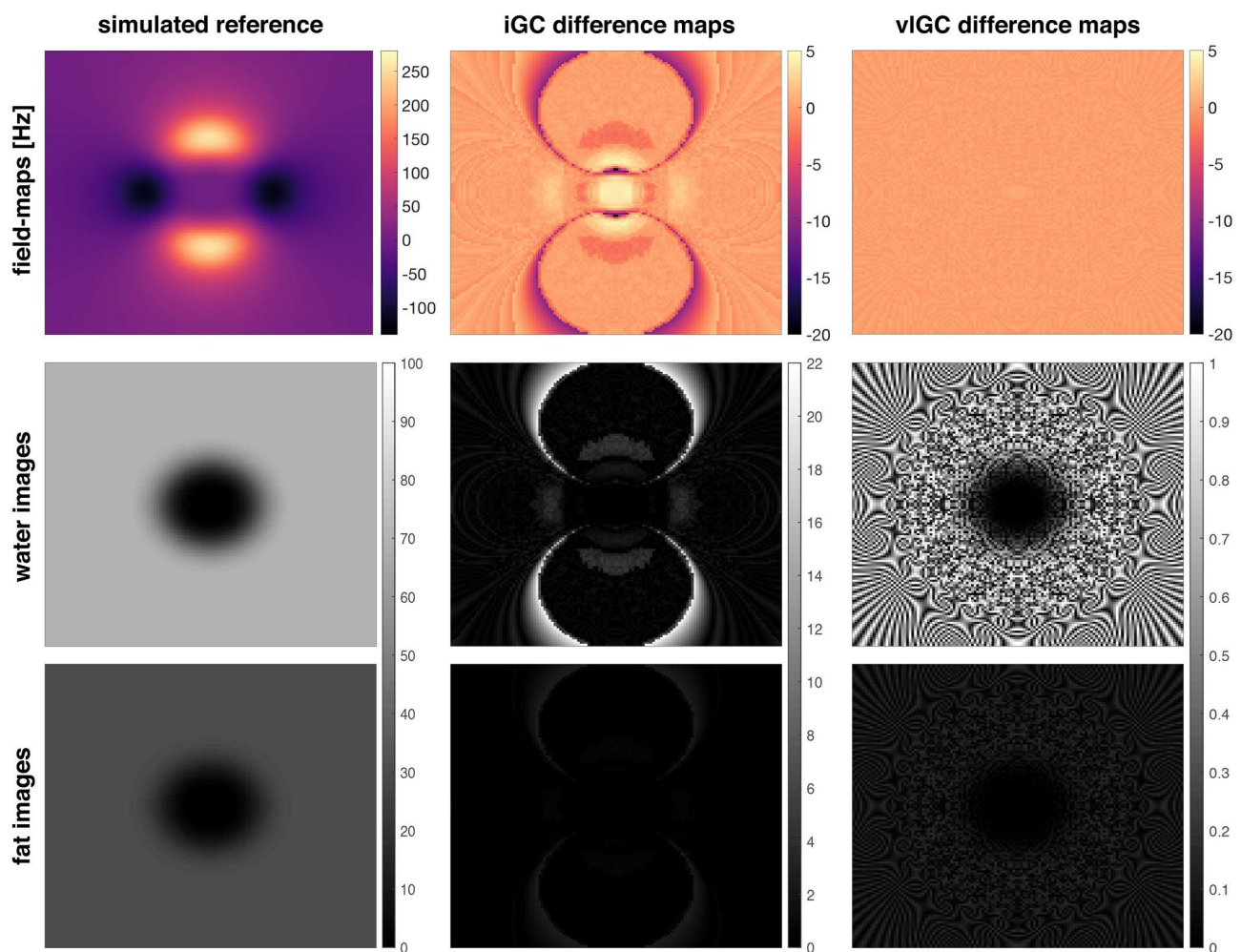


FIGURE 3 Field-mapping (first row), water- (second row) fat (third row) separation results of the numerical phantom with smooth air-tissue interface at the central slice using the iGC and the vIGC. The first column shows the reference water and fat images, the second column shows the difference of the results from the iGC to the reference, and the third column shows difference of the results from the vIGC to the reference. The field-mapping errors in the numerical phantom propagate into water–fat separation, where the error in the iGC method becomes up to 61%, while for the proposed vIGC it stays below 1.4% in the whole volume

phantom. The field-map of the iGC method follows the reference starting at the periphery of the volume until a certain point close to the boundary with the signal void and the errors become then significant until the center of the volume. The field-map of rGOOSE follows the reference for a wider spatial extent but also fails very close to the signal void on one side of the air-tissue interface. Only the field-map of the vIGC follows the reference for the whole volume.

The second row of Figure 4 shows the closed-form ℓ_2 -regularized dipole inversion results for the different field-maps plotted in the first row of Figure 4. The magnetic susceptibility results based on the vIGC are much closer to the ground truth and show greatly reduced streaking artifacts. The corresponding line plot show that the χ -maps based on the iGC method drastically overshoot outside and inside the air-containing signal void. While there is still a significant underestimation of χ values outside the signal void, the results based on rGOOSE already show a significant improvement

over the iGC. However, the field-map jump close to the interface clearly introduces artifacts in the susceptibility map. The vIGCs χ -maps are closest to the reference, compared to the iGC and the rGOOSE method. Figure 5 shows that the simulation depicted in Figure 4 are in close agreement with the experimental measurements of the air bubble phantom. Furthermore, the vIGC is significantly more robust to the strong background field variations introduced by the shimming fields and yields comparable susceptibility values at different shimming settings. The QSM results based on the iGC significantly overestimate the susceptibility of air and include large errors at strong background fields

4.3 | In vivo results

Figure 6 shows the field-mapping results and the corresponding water–fat separated images in one large-FOV

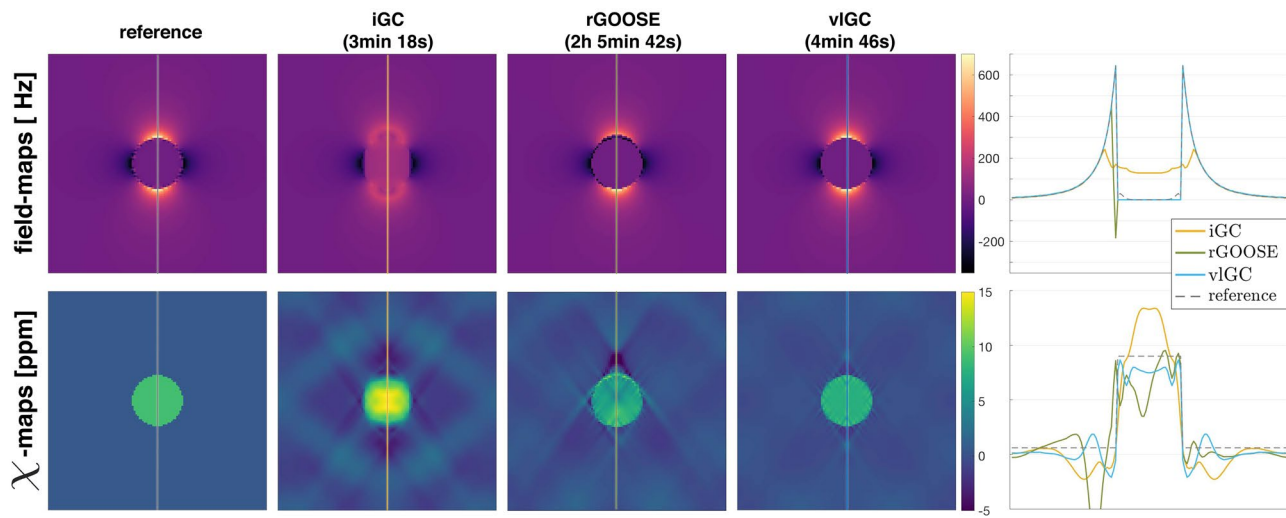


FIGURE 4 Field-mapping (first row) and QSM (second row) results of the numerical simulation with sharp air-tissue interface of an MR-invisible air bubble in an environment with 30% fat fraction using a simple closed-form ℓ_2 -regularized dipole inversion. The time given below each method's name represents the run-time of the respective method. The first column shows the reference field- and susceptibility-map, the second column shows the results from the iGC, the third column shows the results from the rGOOSE and the fourth column the results from the vIGC and the fifth column shows line plots for the field-map and susceptibility-map for all methods. Compared to the iGC the vIGC is able to greatly reduce streaking by correctly estimating field-map values close to the signal void and the shape of the sphere is preserved while the computational cost is only reasonably increased. The rGOOSE is already performing significantly better in the parameter estimation than the iterative graph-cut. However, it suffers from its graph construction leading to a long run-time and a accidental rejection of the correct field-map solution close the signal void in the algorithms default settings

head/neck scan. The vIGC is able to resolve the large dynamic range of 5340 Hz on the shown field-map, without an additional unwrapping step, resolving even the very rapid field-map variation at the bottom of the FOV. The volumetric field-mapping data from the head/neck region of 14 subjects are provided as Supporting Information Video S1-S14. The visual reading of the 14 head/neck datasets yields swaps in the results by the iGC in all subjects obtained by the iGC. Furthermore, the location of the swaps changes significantly along the slice direction. The vIGC shows water-fat swaps in 3 subjects.

Figure 7 shows a lumbar spine with an intradiscal air inclusion. The derived χ -map based on the field-map of the vIGC reveals the true underlying paramagnetic property of the air-like gas (of the order of 9.4 ppm). The χ -map based on the field-map of the iGC indicates a paramagnetic susceptibility source. The presence of the air-inclusion was verified on a computed tomography (CT) scan. The CT scan showed an additional calcification on the top of the FOV, which also results in an MR signal void in the corresponding image of the magnitude of the first echo. QSM based on both field-mapping methods is able to correctly estimate the diamagnetic property of the calcification.

Figure 8 shows field-mapping and QSM results of a second lumbar spine scan with the trabecular bone structure of a spinous process as the region-of-interest (arrow). The estimated QSM maps show first that the field-map estimated by the iGC was very smooth when compared to the vIGC and

second that the smoothed field-map translated to a significant underestimation of the susceptibility values of the cortical bone structure in the ROI.

Figure 9 shows the results of the mean magnetic susceptibility value analysis of the spinous process cortical bone region of the L3 vertebra in the lumbar spine of the 4 scanned volunteers. QSM based on the vIGC yields susceptibility values that are significantly closer to the literature value of cortical bone than QSM based on the iGC. Furthermore, in a repeatability experiment in one subject the mean susceptibility value within the ROI was stable when using the field-map from the vIGC.

5 | DISCUSSION

The present work aimed to develop a method for improved field-mapping in challenging anatomical water-fat regions and to particularly apply the developed method in body applications of QSM. Specifically, this work first proposed a global penalized maximum likelihood cost function with a novel formulation to enforce the data consistency and then introduced the solution of the cost function using a single-min-cut graph-cut on a variable-layer graph that allows to select the same field-map range for each voxel. The work then examined the effect of the field-mapping accuracy on the estimated magnetic susceptibility in particular close to MR signal voids and applied the developed field-mapping method in body QSM of regions enclosing water, fat, and MR signal voids.

Shimming Variation in z-direction

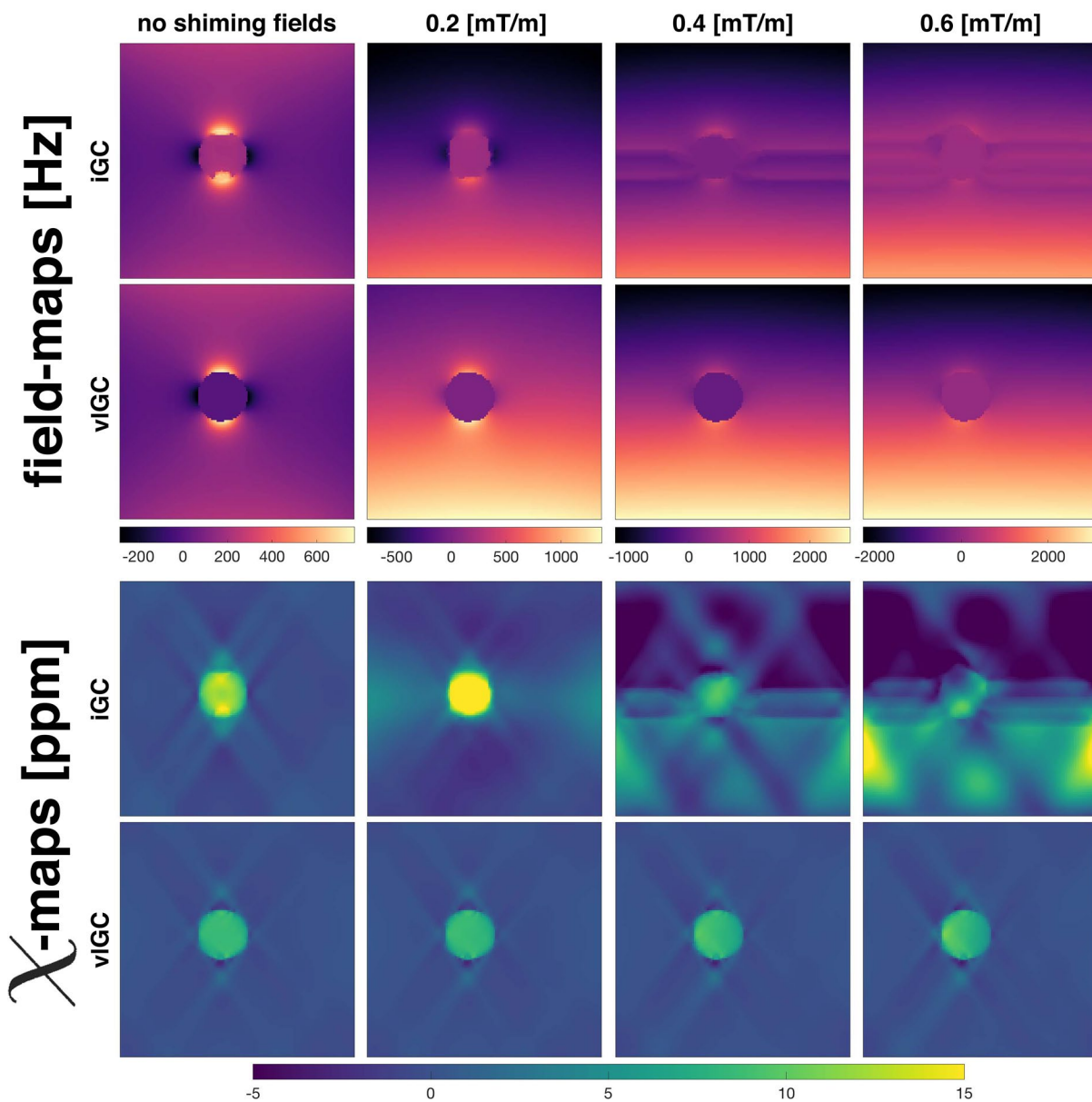


FIGURE 5 Field-mapping (first two rows) and QSM (last two rows) results of the experimental air bubble phantom with sharp air-water interface and varying shim fields. The iGC is challenged in estimating the sharp boundary of the phantom estimating non-physical values within the signal void. Furthermore, the iGC is only able to pick up the background field variation for the first shim field setting of 0.2 mT/m and is showing wraps at higher shim field settings. The difference of the vIGC field-map and of the iGC field-map for the first shim setting is in the order of 440 Hz and refers to a total swap for the iGC. QSM based on the vIGC yields homogeneous and robust results for all shim field strengths while slightly underestimating the susceptibility within the air inclusion. QSM based on the iGC shows a strong dependence on the underlying shim field strength

Since the vIGC will always find the global minimum of the cost function,³⁰ the correct estimation of the field-map and the occurrence of resulting water–fat swaps only depend on the design of the cost function. Consequently, the proposed field-mapping method introduces some important novel features for solving the water–fat problem using graph-cuts. First, the vIGC algorithm enforces the data consistency solely by the extraction of the minima from the voxel-wise

estimates. In the iGC and in the rGOOSE methods,^{20,25} the voxel-wise residual is used for data consistency. The presently proposed enforcement of the data consistency by extracting only the local minima equalizes the significance of all voxels in the volume in reference to the smoothness constraint. The ability of the vIGC to find the global minimum of the cost function potentially comparing a manifold of voxel-wise solutions is a strong advantage when compared

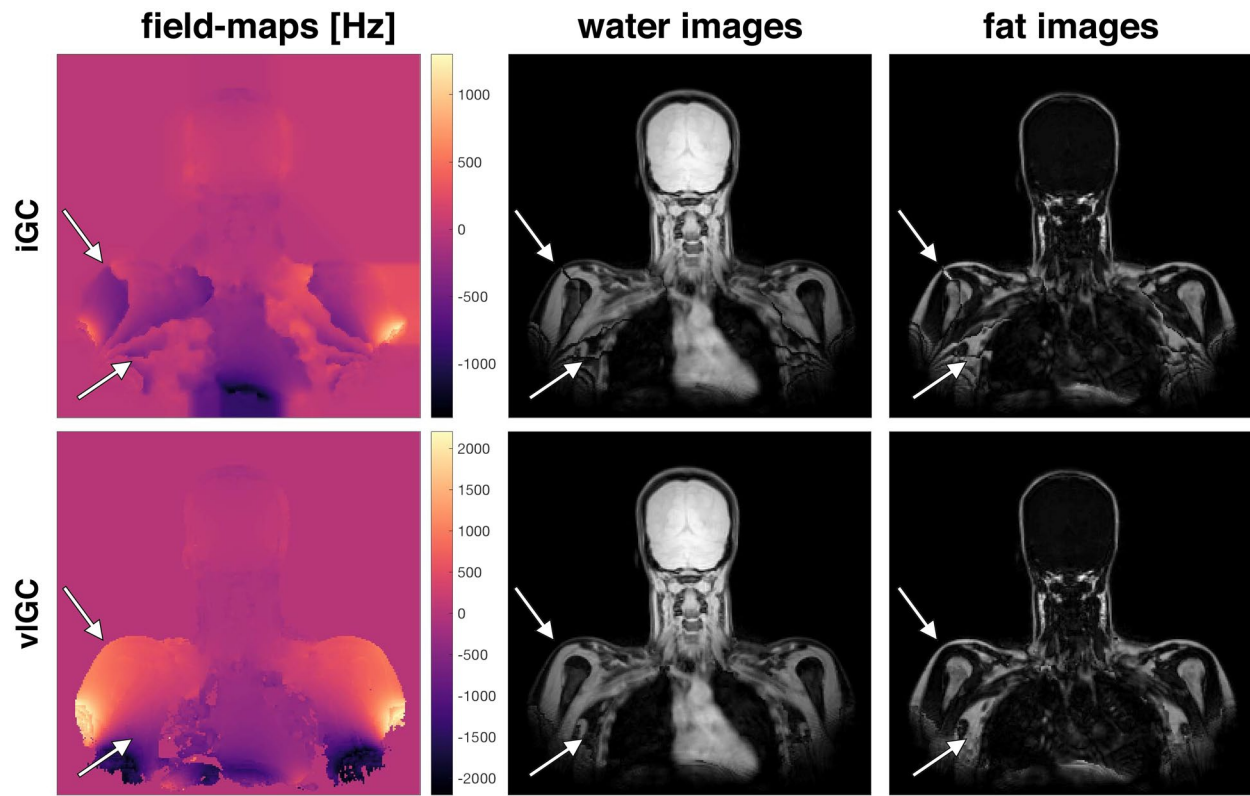


FIGURE 6 Field-mapping (first column) and water- (second column) fat (third column) separation results in a large FOV head/neck region scan. The first row shows the results from the iGC and the second row the results from the vIGC. The vIGC is able to resolve the large dynamic range of 5340 Hz on the shown field-map resolving even the very rapid field-map variation at the bottom of the FOV. The iGC yields a significantly reduced dynamic range and shows phase-wraps. The phase-wraps propagate into the water–fat separated images (arrows). Similar datasets are provided in the supplementary material as videos showing the methods comparison across slices

to the iGC. In the iGC, for each voxel only two field-map candidates are taken and a graph-cut is used to solve the cost function value in a so-called jump move. If the cost function decreases, the field-map candidate is taken. This procedure is repeated until a defined convergence criterion is met. In contrast to the vIGC, the iGC needs to perform several graph-cuts in several jump move steps. While each graph-cut is guaranteed to find the globally optimal solution to the corresponding binary sub-problem, this is not necessarily true for the global cost function. Furthermore, since in the iGC the candidates are not restricted to be only local minima of the voxel-wise field-map estimate, the field-map estimation is inherently dependent on the use of an additional data consistency term.

Second, the vIGC requires an a priori defined field-map sampling interval. Specifically, the present work first defined an optimal sampling interval over which the voxel-wise cost function Equation (5) needs to be sampled in order to obtain phase unwrapped field-map solutions in the whole volume. Overestimating the size of the field-map sampling interval still leads to the global minimum of the cost function, but with a longer run-time of the graph routine. Since \hat{f}_B is unknown, $f_{\text{interval}} = |\max(\hat{f}_B) - \min(\hat{f}_B)|$ must be estimated with prior

knowledge. Since overestimating the size of the sampling interval f still leads to the global minimum of the cost function, one can choose the sampling interval in this first step arbitrarily large. For $f > f_{\text{interval}} + n \cdot f_{\text{period}}$, $n \in \mathbb{N}$, Equation (6) becomes periodic with $n+1$ solutions. Since the graph-cut algorithm will yield only one solution, the graph-cut solution can lead to field-maps not centered around zero but in a different period of the field-map estimate. Which exact solution is yielded simply depends on rounding and numerical errors. However, all above solutions are correct and can be brought into the same period centered around zero by computing the mean of the field-map estimate modulo the period length.

Third, the vIGC uses a graph construction enabling accelerated computations. The introduced advancements in the graph construction related to the variable-layer architecture and the inclusion to the graph of signal-only regions lead to the smallest possible size of the graph for a given a priori known sampling interval f_{total} . After the field-map sampling interval is defined, it is important to point out that the variable-layer graph architecture significantly reduces the number of nodes per voxel compared to formerly proposed single-min-cut graph-cut algorithms. Usually, in regions with high SNR there are only two minima per period

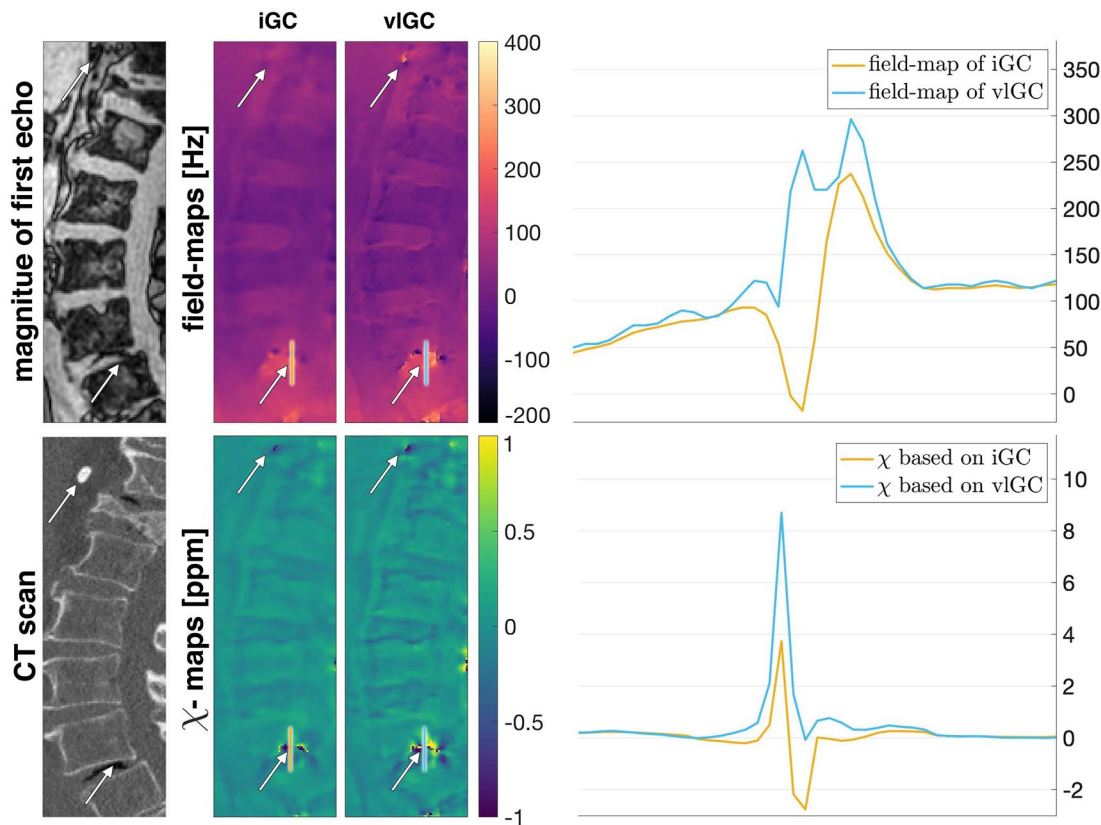


FIGURE 7 Field-mapping (first row) and susceptibility (second row) results in a pathological lumbar spine with a calcification at the top of the FOV and a intradiscal gas inclusion at the bottom leading to an MR signal void region, both highlighted by arrows. The first column shows the magnitude of the first echo, the second column shows the results from the iGC, the third column shows the result from the vIGC, and the last column shows line plots over the intradiscal gas inclusion. All susceptibility maps can correctly estimate the calcification to be diamagnetic. The line profiles over the intradiscal gas inclusion illustrate the significantly different values yielded by the iGC and the vIGC in this region. Only the vIGC is able to reveal the true underlying paramagnetic property of the air-like gas (of the order of 9.4 ppm). The susceptibility map based on the field-maps of the iGC falsely indicates the air inclusion to be mainly diamagnetic. The result is verified by the CT scan

in C. Only in voxels with low SNR there are commonly more. Compared to GOOSE²⁴ and rGOOSE,²⁵ the size of the graph using the vIGC can be reduced by approximately a factor of 50 and 4 for voxels with high SNR, respectively, and by factor of 200 and 16 for voxels with low SNR, respectively. Such a reduction in the graph size results in a decrease of the required run-time by an order of magnitude. However, in the case of strong background field-map variations as shown in Figure 6 the vIGC could potentially be combined with a phase-unwrapping methods such as³⁸ or coarse to fine grid approaches as used in³⁹ in order to further reduce the run-time. The variable-layer graph construction is also a significant advantage over the rGOOSE method that only allows for the same amount of minima per voxel for the whole volume. However, when the same field-map range is sampled for the voxel-wise field-map estimate, the number of minima in a voxel depends on the SNR and can consequently vary voxel by voxel. Although rGOOSE guarantees convergence to its global minimum, the restriction in the graph-construction can lead either to an accidental

miss of the correct voxel field-map estimate or to a significant increase in run-time making the method infeasible for clinical datasets of large sizes. Furthermore, the vIGC has been demonstrated to be able to directly yield non-wrapped field-maps. An accurate and inherently non-wrapped field-map is particularly important for quantitative susceptibility mapping. Field-map errors and wraps are expected to translate in strong susceptibility artifacts.¹⁶ Since QSM is based on the field-map estimate, errors in the field-map estimation propagate into the susceptibility maps as demonstrated in Figures 4 and 5. Using the proposed method, an erroneous algorithmic step in the QSM processing pipeline can be circumvented. It has also been demonstrated that despite the long-range effect of the dipole field and the corresponding kernel,¹ field-map values at the border to an MR signal void containing a strong susceptibility source like air are important to map correctly in order to obtain correct susceptibility values. Correct field-map values at a certain distance to the signal void and data weighting are not sufficient. Therefore, it becomes essential to accurately estimate field-map values

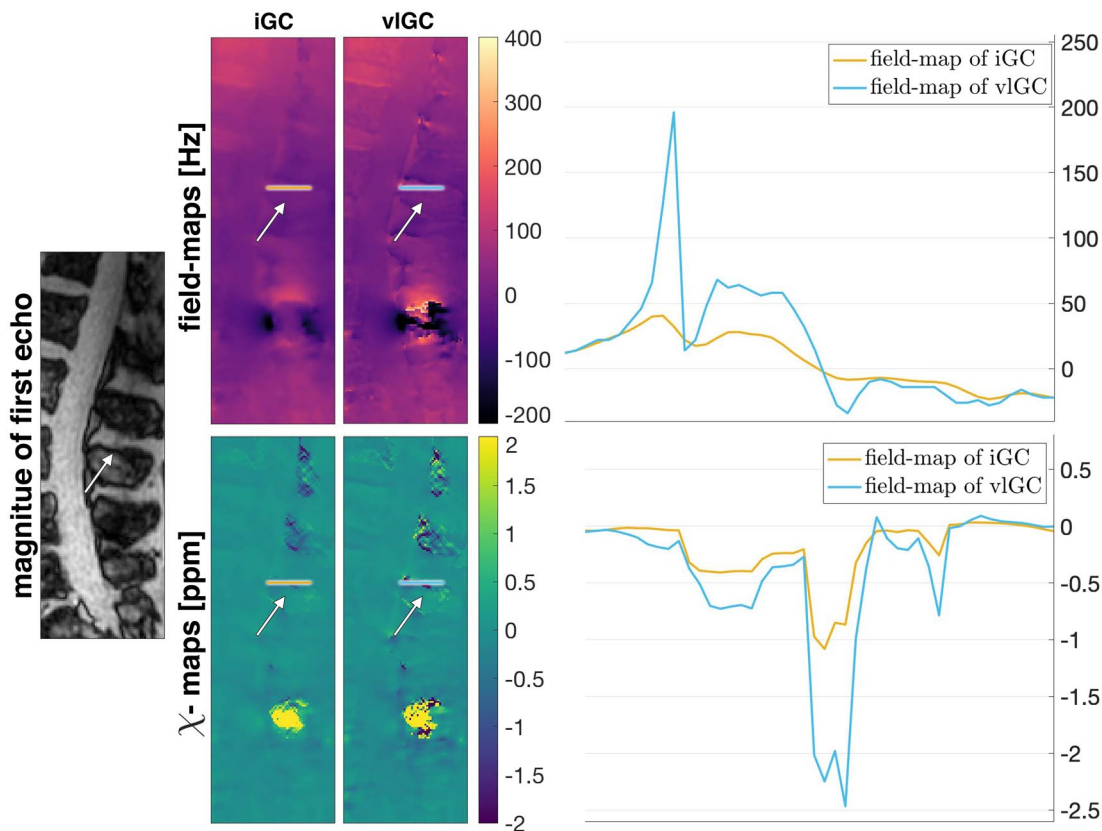


FIGURE 8 Field-mapping (first row) and susceptibility (second row) results in the spinous process cortical bone region-of-interest (arrows). The first column shows the magnitude of the first echo, the second column shows the results from the iGC, the third column shows the result from the vIGC, and the last column shows line plots over the cortical bone region. QSM based on the vIGC is able to estimate the literature susceptibility value of bone of approximately -2 ppm at the spinous process while the QSM based on the iGC yields significantly reduced susceptibility values of only -1 ppm

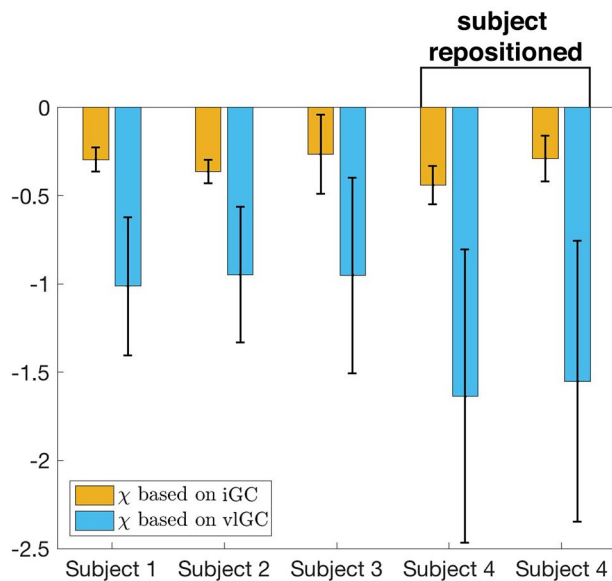


FIGURE 9 Mean magnetic susceptibility value analysis of the spinous process cortical bone region-of-interest at the L3 in 4 subjects as well as a repeatability test of the fourth subject by re-positioning and re-scanning the subject. QSM based on the iGC yields in all subjects a significant underestimation of susceptibility values of cortical bone while susceptibility values based on the vIGC are significantly closer to the literature value

as close as possible to an MR signal void. This conclusion is supported by the spine with an intradiscal air inclusion. QSM based on the vIGC is able to reveal the strong paramagnetic susceptibility value of the air-like gas. The correct estimation of the air inclusion magnetic susceptibility was not achieved with the field-maps of the iGC. Furthermore, the vIGC is able to estimate susceptibility values much closer to the literature value in a cortical bone region-of-interest in several subjects as shown in Figures 8 and 9.

The present work has some limitations. In order to benefit from the full 3D neighborhood information, the graph for the whole volume needs to be loaded into the RAM, which can be in the order of several 10 GiB. Furthermore the graph-cut itself is intrinsically not parallelizable without the loss of accuracy⁴⁰⁻⁴² and the run-time drastically scales with the number of nodes. Due to possible computation time restrictions with big datasets, a chunked minimization can be applied, which does not only minimize partial volumes (eg, slices) independently, but applies the smoothness constraint from Equation (6) from one chunk to the adjacent. A more detailed description of the chunked minimization is provided in the supplementary material. However, the run-time for a clinical relevant dataset like in the presented lumbar

spine is in the reasonable order of 5 minutes. Second, the selection of the size of the neighborhood $N(\mathbf{r})$ of the global cost function has not been optimized. The 6-connected von Neumann voxel neighborhood including the adjacent voxel in x -, y -, z -direction was presently used but a 26-neighborhood would be also possible. A larger neighborhood translates into an increased importance of the spatial smoothness term in Equation (6), which has to be considered. Since only local minima that have a predefined distance in frequency are extracted, the global optimal field-map is piece-wise constant with respect to the size of the penalization term and therefore the global minimum might not be effected. Third, studies on field-map and QSM generally have the limitations that results can only heuristically be evaluated in the water–fat domain or be compared to literature values for susceptibility values. The present work showed that the present methodology yields robust field-map and susceptibility results in numerical simulations of air-tissue geometries, in a phantom scanned at different settings and in vivo spine measurements. However, the present methodology would strongly benefit from a large scale validation of its performance in estimating magnetic susceptibility in further body QSM applications.

6 | CONCLUSION

A single-min-cut graph-cut field-mapping method with a variable-layer construction was proposed for field-mapping in body water–fat regions. The proposed method shows the following significant improvements over an iterative graph-cut field-mapping method: (a) it can resolve strong field-mapping variations close to MR signal voids, (b) it performs significantly better in regions with strong field-map variation and high R_2^* values, (c) it can directly yield non-smooth field-maps like a voxel-wise method, and (d) it significantly improves subsequently performed quantitative susceptibility mapping particularly in areas close to MR signal voids.

ACKNOWLEDGMENT

The authors thank the contributors of the ISMRM Fat–Water Toolbox for the publication of their algorithm implementations. The authors also thank Dr. Alexandra Gersing and Dr. Thomas Baum for discussions related to the patient spine in vivo results and Dr. Jakob Meineke for helpful discussions regarding the QSM processing. The present work was supported by the European Research Council (grant agreement No 677661, ProFatMRI). This work reflects only the authors' view and the EU is not responsible for any use that may be made of the information it contains. The authors also acknowledge research support from Philips Healthcare. Open access funding enabled and organized by Projekt DEAL.

DATA AVAILABILITY STATEMENT

Example MATLAB code of our implementation of the proposed method will be made freely available for download at <https://gitlab.com/christofboehm/fieldmap-graph-cut>.

ORCID

Christof Boehm  <https://orcid.org/0000-0003-1321-5804>
Maximilian N. Diefenbach  <https://orcid.org/0000-0002-5581-885X>

TWITTER

Christof Boehm  @BoehmChristof

REFERENCES

1. Wang Y, Liu T. Quantitative susceptibility mapping (QSM): decoding MRI data for a tissue magnetic biomarker. *Magn Reson Med.* 2014;73:82–101.
2. Liu C, Li W, Tong KA, Yeom KW, Kuzminski S. Susceptibility-weighted imaging and quantitative susceptibility mapping in the brain. *J Magn Reson Imaging.* 2014;42:23–41.
3. EskreisWinkler S, Zhang Y, Zhang J, et al. The clinical utility of qsm: disease diagnosis, medical management, and surgical planning. *NMR Biomed.* 2016;30:e3668.
4. Sun H, Seres P, Wilman A. Structural and functional quantitative susceptibility mapping from standard fMRI studies. *NMR Biomed.* 2016;30:e3619.
5. Sharma SD, Hernando D, Horng DE, Reeder SB. Quantitative Susceptibility mapping in the abdomen as an imaging biomarker of hepatic iron overload. *Magn Reson Med.* 2014;74:673–683.
6. Lin H, Wei H, He N, et al. Quantitative susceptibility mapping in combination with water–fat separation for simultaneous liver iron and fat fraction quantification. *Eur Radiol.* 2018;28:3494–3504.
7. Jafari R, Sheth S, Spincemaille P, et al. Rapid automated liver quantitative susceptibility mapping. *J Magn Reson Imaging.* 2019;50:725–732.
8. Straub S, Laun FB, Emmerich J, et al. Potential of quantitative susceptibility mapping for detection of prostatic calcifications. *J Magn Reson Imaging.* 2016;45:889–898.
9. Wei H, Lin H, Qin L, et al. Quantitative susceptibility mapping of articular cartilage in patients with osteoarthritis at 3t. *J Magn Reson Imaging.* 2018;49:1665–1675.
10. Dimov AV, Liu Z, Spincemaille P, Prince MR, Du J, Wang Y. Bone quantitative susceptibility mapping using a chemical species-specific R_2^* signal model with ultrashort and conventional echo data. *Magn Reson Med.* 2017;79:121–128.
11. Diefenbach MN, Meineke J, Ruschke S, Baum T, Gersing A, Karampinos DC. On the sensitivity of quantitative susceptibility mapping for measuring trabecular bone density. *Magn Reson Med.* 2019;81:1739–1754.
12. Wang Y, Spincemaille P, Liu Z, et al. Clinical quantitative susceptibility mapping (qsm): biometal imaging and its emerging roles in patient care. *J Magn Reson Imaging.* 2017;46:951–971.
13. Diefenbach MN, Van A, Meineke J, et al. On the sensitivity of bone marrow magnetic susceptibility and R_2^* on trabecular bone microstructure. In Proceedings 26th Annual Meeting International Society for Magnetic Resonance in Medicine, Paris, France; 2018:0533.
14. Colgan TJ, Knobloch G, Reeder SB, Hernando D. Sensitivity of quantitative relaxometry and susceptibility mapping to microscopic iron distribution. *Magn Reson Med.* 2020;83:673–680.

15. Dimov AV, Liu T, Spincemaille P, et al. Joint estimation of chemical shift and quantitative susceptibility mapping (chemical Qsm). *Magn Reson Med.* 2014;73:2100-2110.
16. Bechler E, Stabinska J, Wittsack H. Analysis of different phase unwrapping methods to optimize quantitative susceptibility mapping in the abdomen. *Magn Reson Med.* 2019;82:2077-2089.
17. Fortier V, Levesque IR. Phase processing for quantitative susceptibility mapping of regions with large susceptibility and lack of signal. *Magn Reson Med.* 2018;79:3103-3113.
18. Yu H, Reeder SB, Shimakawa A, Brittain JH, Pelc NJ. Field map estimation with a region growing scheme for iterative 3-point water-fat decomposition. *Magn Reson Med.* 2005;54:1032-1039.
19. Hernando D, Haldar JP, Sutton BP, Ma J, Kellman P, Liang ZP. Joint estimation of water/fat images and field inhomogeneity map. *Magn Reson Med.* 2008;59:571-580.
20. Hernando D, Kellman P, Haldar JP, Liang ZP. Robust water/fat separation in the presence of large field inhomogeneities using a graph cut algorithm. *Magn Reson Med.* 2009;63:NA-NA.
21. Tsao J, Jiang Y. Hierarchical ideal: fast, robust, and multiresolution separation of multiple chemical species from multiple echo times. *Magn Reson Med.* 2012;70:155-159.
22. Berglund J, Johansson L, Ahlström H, Kullberg J. Three-point Dixon method enables whole-body water and fat imaging of obese subjects. *Magn Reson Med.* 2010;63:1659-1668.
23. Hu HH, Börnert P, Hernando D, et al. Ismrm workshop on fat-water separation: insights, applications and progress in MRI. *Magn Reson Med.* 2012;68:378-388.
24. Cui C, Wu X, Newell JD, Jacob M. Fat water decomposition using globally optimal surface estimation (goose) algorithm. *Magn Reson Med.* 2014;73:1289-1299.
25. Cui C, Shah A, Wu X, Jacob M. A rapid 3d fat-water decomposition method using globally optimal surface estimation (R-GOOSE). *Magn Reson Med.* 2017;79:2401-2407.
26. Yu H, Shimakawa A, McKenzie CA, Brodsky E, Brittain JH, Reeder SB. Multiecho water-fat separation and simultaneous R_2^* estimation with multifrequency fat spectrum modeling. *Magn Reson Med.* 2008;60:1122-1134.
27. Bydder M, Yokoo T, Hamilton G, et al. Relaxation effects in the quantification of fat using gradient echo imaging. *Magn Reson Imaging.* 2008;26:347-359.
28. Hernando D, Kellman P, Haldar J, Liang ZP. Estimation of water/fat images, B_0 field map and T_2^* map using VARPRO. In *ISMRM 16th Scientific Meeting & Exhibition, Toronto, Canada*, 2008:1517.
29. Lu W, Hargreaves BA. Multiresolution field map estimation using golden section search for water-fat separation. *Magn Reson Med.* 2008;60:236-244.
30. Shah A, Abramoff MD, Wu X. Optimal surface segmentation with convex priors in irregularly sampled space. *Med Image Anal.* 2019;54:63-75.
31. Boykov Y, Kolmogorov V. An experimental comparison of min-cut/max-flow algorithms for energy minimization in vision. *IEEE Trans Pattern Anal Mach Intelligence.* 2004;26:1124-1137.
32. Griffiths DJ. *Introduction to electrodynamics*, 4th ed. Boston, MA: Pearson, 2013. Re-published by Cambridge University Press in 2017.
33. Ren J, Dimitrov I, Sherry AD, Malloy CR. Composition of adipose tissue and marrow fat in humans by 1 h Nmr at 7 Tesla. *J Lipid Res.* 2008;49:2055-2062.
34. Bilgic B, Chatnuntawech I, Fan AP, et al. Fast image reconstruction With L2-regularization. *J Magn Reson Imaging.* 2013;40:181-191.
35. Ruschke S, Eggers H, Kooijman H, et al. Correction of phase errors in quantitative water-fat imaging using a monopolar time-interleaved multi-echo gradient echo sequence. *Magn Reson Med.* 2016;78:984-996.
36. Zhou D, Liu T, Spincemaille P, Wang Y. Background field removal by solving the Laplacian boundary value problem. *NMR Biomed.* 2014;27:312-319.
37. Diefenbach MN, Van A, Meineke J, et al. Vertebral column quantitative susceptibility mapping using joint background field removal and dipole inversion. In Proceedings 26th Annual Meeting International Society for Magnetic Resonance in Medicine, Paris, France; 2018:0191.
38. Dong J, Chen F, Zhou D, Liu T, Yu Z, Wang Y. Phase unwrapping with graph cuts optimization and dual decomposition acceleration for 3d high-resolution MRI data. *Magn Reson Med.* 2016;77:1353-1358.
39. Berglund J, Skorpil M. Multi-scale graph-cut algorithm for efficient water-fat separation. *Magn Reson Med.* 2016;78:941-949.
40. Vineet V, Narayanan PJ. CUDA cuts: fast graph cuts on the GPU. In *2008 IEEE Computer Society Conference on Computer Vision and Pattern Recognition Workshops, Anchorage, USA*, 2008;6:1-8.
41. Strandmark P, Kahl F. Parallel and distributed graph cuts by dual decomposition. In *2010 IEEE Computer Society Conference on Computer Vision and Pattern Recognition, San Francisco, CA, USA*, 2010;6:2085-2092.
42. Yu M, Shen S, Hu Z. Dynamic parallel and distributed graph cuts. *IEEE Trans Image Process.* 2016;25:5511-5525.

SUPPORTING INFORMATION

Additional supporting information may be found online in the Supporting Information section.

VIDEO S1. Volunteer 1: Field-mapping (first column) and water- (second column) fat (third column) separation results in large FOV head/neck region scan. The first row shows the results from the iGC and the second row the results from the vIGC. The vIGC is able to resolve the large dynamic range of the field-map in the subject resolving even the very rapid field-map variation at the bottom of the FOV. The iGC yields a significantly reduced dynamic range of the field-map and shows water-fat swaps. The location of water-fat swaps in the iGC results strongly varies along slice direction

VIDEO S2. Volunteer 2: Field-mapping (first column) and water- (second column) fat (third column) separation results in large FOV head/neck region scan. The first row shows the results from the iGC and the second row the results from the vIGC. The vIGC is able to resolve the large dynamic range of the field-map in the subject resolving even the very rapid field-map variation at the bottom of the FOV. The iGC yields a significantly reduced dynamic range of the field-map and shows water-fat swaps. The location of water-fat swaps in the iGC results strongly varies along slice direction

VIDEO S3. Volunteer 3: Field-mapping (first column) and water- (second column) fat (third column) separation results

shows water–fat swaps. The location of water–fat swaps in the iGC results strongly varies along slice direction. The vIGC and the iGC show a water–fat swap in the upper part of the brain

VIDEO S14. Volunteer 14: Field-mapping (first column) and water– (second column) fat (third column) separation results in large FOV head/neck region scans. The first row shows the results from the iGC and the second row the results from the vIGC. The vIGC is able to resolve the large dynamic range of the field-map in the subject resolving even the very rapid field-map variation at the bottom of the FOV. The iGC yields a significantly reduced dynamic range of the field-map and

shows water–fat swaps. The location of water–fat swaps in the iGC results strongly varies along slice direction. The vIGC and the iGC show a water–fat swap in the upper part of the brain

How to cite this article: Boehm C, Diefenbach MN, Makowski MR, Karampinos DC. Improved body quantitative susceptibility mapping by using a variable-layer single-min-cut graph-cut for field-mapping. *Magn Reson Med.* 2021;85:1697–1712.
<https://doi.org/10.1002/mrm.28515>